

Accepted Manuscript

## *Geological Society, London, Special Publications*

### Some petrographic and mineralogical diagnostics of sandstone intrusions

Andrew Hurst, Wiktor Luzinski, Gustavo Zvirtes, Tony Scott, Mario Vigorito, Andrew Morton & Feng Wu

DOI: <https://doi.org/10.1144/SP493-2018-063>

Received 20 March 2018

Revised 27 January 2020

Accepted 18 May 2020

© 2020 The Author(s). Published by The Geological Society of London. All rights reserved. For permissions: <http://www.geolsoc.org.uk/permissions>. Publishing disclaimer: [www.geolsoc.org.uk/pub\\_ethics](http://www.geolsoc.org.uk/pub_ethics)

When citing this article please include the DOI provided above.

#### **Manuscript version: Accepted Manuscript**

This is a PDF of an unedited manuscript that has been accepted for publication. The manuscript will undergo copyediting, typesetting and correction before it is published in its final form. Please note that during the production process errors may be discovered which could affect the content, and all legal disclaimers that apply to the book series pertain.

Although reasonable efforts have been made to obtain all necessary permissions from third parties to include their copyrighted content within this article, their full citation and copyright line may not be present in this Accepted Manuscript version. Before using any content from this article, please refer to the Version of Record once published for full citation and copyright details, as permissions may be required.

## **Some petrographic and mineralogical diagnostics of sandstone intrusions**

ANDREW HURST<sup>1</sup>, WIKTOR LUZINSKI<sup>1</sup>, GUSTAVO ZVIRTES<sup>1</sup>, TONY SCOTT<sup>1,2</sup>,  
MARIO VIGORITO<sup>1,3</sup>, ANDREW MORTON<sup>1,4</sup> & FENG WU<sup>1,5</sup>

<sup>1</sup>*University Aberdeen, Department of Geology and Petroleum Geology, King's  
College, Aberdeen, AB24 3UE, UK*

<sup>2</sup>*EquinorASA, Reservoir Modeling, PTEC GGP GM - ST-GR B3, Forus, Stavanger,  
Norway*

<sup>3</sup>*Equinor ASA, Exploration Norway, EXP EE GCQ – ST-FV E3, Forus, Stavanger,  
Norway*

<sup>4</sup>*HM Research Associates Ltd, Giddanmu, Musselwick Road, St Ishmaels SA62 3TJ,  
UK*

<sup>5</sup>*School of Geoscience and Technology, Southwest Petroleum University, Chengdu,  
610500, China*

*Corresponding author (e-mail: [ahurst@abdn.ac.uk](mailto:ahurst@abdn.ac.uk))*

**Abstract:** Sandstone intrusions in giant injection complexes are characterised by texturally immature sand with common micro-fractured framework grains. Individual micro-fractures are distinctive in geometry and unaligned within or between grains thus differentiating them from micro-fractures formed by shock metamorphism or tectonics. Individual grains preserve histories of multiple impacts during sand injection. Micro-fracture geometry and their textural association makes them diagnostic of high energy inter-granular collisions during sand injection. Mudstone clasts have sand propped micro-fractures associated with hydraulic fracturing and individual sand grains embedded in clasts by corrasion, which is diagnostic of high grain-velocity. Heavy mineral assemblages record abrasion of apatite and hydrodynamic segregation of zircon (both relative to abundance of tourmaline) upward through the injection complex. Granular abrasion and hydrodynamic segregation are consistent with turbulent flow during sand injection. Collectively the petrographic and mineralogical data support the interaction of high velocity grains in turbulent flow during sand injection in which the granular content is likely to be dilute.

Despite the growing significance of giant sand injection complexes in oilfield exploration and development very little is published about their petrographic and mineralogical characteristics. There is promise however that petrographic characteristics are diagnostic of sandstone intrusions, and implicitly a product of the process of sand injection (Kawakami & Kawamura 2002; Scott et al. 2009; Bouroullec & Pyles 2010). Heavy mineralogy is amenable to diagnosing subsurface relationships between sandstone intrusions and depositional parent units, henceforth termed parent units (Morton et al. 2014). Petrography and mineralogy become increasingly significant when differentiation between sandstone intrusions and parent units are challenging even when good outcrop or continuous core are available. While not overlooking the value of internal structures as characteristic, and sometimes diagnostic, of sandstone intrusions (Dixon et al. 1995; Duranti & Hurst 2004; Scott et al. 2009; Hurst et al. 2011) petrographic and mineralogical data are inherently first-order indices of inter-granular interaction during sand injection.

The Panoche Giant Injection Complex (PGIC, Vigorito et al. 2008; Vigorito & Hurst 2010) and Tumey Giant Injection Complex (TGIC, Zvirtes et al. 2019) are by far the largest known exposures of giant sand injection complexes and are used routinely as analogues in subsurface interpretation (Briedis et al. 2007; Schwab et al. 2014; Skjaerpe et al. 2018; Grippa et al. 2019; Satur et al. 2020). The PGIC outcrops in an area of almost 400 km<sup>2</sup> (Vigorito & Hurst 2010), which combined with subsurface occurrence extends over more than 1,500 km<sup>2</sup>. Outcrop and subsurface occurrence of the TGIC is probably more extensive but remains unquantified. Individual PGIC outcrop typically has exposure from below the shallowest parent unit for sand, through the intrusive complex to the palaeo-seafloor (Vigorito & Hurst 2010). Large-

scale features regularly identified on seismic surveys such as saucer and wing geometry intrusions form km-scale exposure (Hurst & Vigorito 2017).

Sand fluidization and injection occur when severe overpressure that locally exceeds the lithostatic gradient in the shallow crust, causes the propagation of hydraulic fractures and induces sand fluidisation into dilated fractures from adjacent depositional sandstones (Duranti & Hurst 2004; Vigorito & Hurst 2010; Hurst et al. 2011). Fluidised sand flow is interpreted to be high velocity, at least  $1 \text{ ms}^{-1}$  (Allen 1984) and during sand injection possibly exceeding  $10 \text{ ms}^{-1}$ , highly turbulent and erosive, and with dilute granular suspensions (Duranti 2007; Hurst et al. 2011). When giant sand injection complexes form, at least  $10^3 \text{ km}^3$  sand is injected, and hydraulic fractures often reach a palaeo-surface, for example a palaeo-seafloor where fluidised sand extrudes forming sand extrudites (Hurst et al. 2006). If the location of the palaeo-surface (seafloor) and the depth to the top of parent unit are known, estimation of the thickness of the injection complex is possible; which for giant injection complexes is typically in the range of 0.5 km to 1.7 km (Vigorito & Hurst 2010).

The mechanical stability of grains and their hydrodynamic fractionation modify grains and grain assemblages during transport and determine their surface texture and propensity to fracture (Margolis & Krinsley 1974). Abrasion is the dominant process in low-velocity, low-turbulent flow with high grain content, whereas grain breakage (fracture) is more prevalent as grain velocity and turbulence increase and grain content is more dilute. During sand injection inter-granular collisions are of specific interest and preserve evidence of impact and corrasion as responses to high-velocity grains in dilute granular flow (Scott et al. 2009). Inter-granular collisions may increase the silt fraction by grain comminution, a significant reason for sandstone

intrusions typically having lower porosity and permeability than their otherwise similar parent units (Duranti et al. 2002; Duranti & Hurst 2004; Briedis et al. 2007; Lonergan et al. 2007). Hydrodynamic fractionation of heavy minerals occurs during flow (Dietz 1973; Komar 2007; Garzanti et al. 2008) and the density segregation of heavy minerals is known to occur throughout the overall vertical fluid-rise in a giant injection complex (Hurst et al. 2017).

To be of diagnostic value, petrographic and mineralogical characteristics need to be easily identifiable, clearly related to their process of formation, and wherever possible quantified. Where the physical relationships between parent units and sandstone intrusions are limited, obscure or absent, petrographic and mineralogical characteristics may have lithostratigraphic significance (Morton et al. 2014). This paper aims to demonstrate the potential diagnostic significance of some petrographic and mineralogical characteristics when identifying sandstone intrusions and their implications for understanding the process of sand injection. Heavy mineral assemblages, originally studied to elucidate lithostratigraphy, are re-investigated as indicators of abrasion and hydrodynamic segregation during sand injection. Detailed evaluation of the genetic significance of the features is to some extent already described (Scott et al. 2009; Hurst et al. 2011; Hurst et al. 2017; Zvirtes et al. 2019) and are the subject of on-going research.

### **Study areas and methods**

Data are acquired from two giant injection complexes, the Panoche Giant Injection Complex (PGIC, Danian, Vigorito et al. 2008) and the Tumey Giant Injection Complex (TGIC, mid-Eocene, Zvirtes et al. 2019) that are remarkably well exposed and good as analogues in sub-surface interpretation. Data were re-examined from

earlier work on the Santa Cruz Mudstone (late Miocene, Scott et al. 2009). Detailed sedimentary logs are available from all areas together with geological maps. Biostratigraphy and lithostratigraphy are well constrained in the PGIC (Ingersoll 1979; McGuire 1988; Diblee 2007; Vigorito et al. 2008) and TGIC (Bartow & Nilsen 1990; Bartow 1991; Zvirtes et al. 2019) and vertical and lateral exposure is extensive. In the Santa Cruz Mudstone bio- and litho-stratigraphy are less well-constrained, individual exposures are much smaller and in a much smaller overall area (Thompson et al. 1998; Boehm & Moore 2002; Scott et al. 2009). All samples were collected from outcrop where the injected origin is incontrovertible and distinct from depositional sandstone. Total thin sections of sandstone examined from the injection complexes are: PGIC and TGIC, 256 samples; Santa Cruz, 27 samples (from the Yellowbank Creek locality, Scott et al. 2009).

Thin section petrography, back-scattered and scanning electron microscopy (BSEM and SEM), or a combination of these, were used for textural characterisation of samples. One sample was analysed using a micro-CT (MCT) scanner (Wu et al. 2018). Heavy mineral fractions were separated using density segregation and minerals were identified using the criteria of Mange & Maurer (1992). Heavy minerals in the silt-size fraction were examined, which is approximately the hydraulic equivalent of fine- to medium-grained quartzo-feldspathic sand and typically used in heavy mineral lithostratigraphic investigations (Hurst & Morton 1988; Morton & Hallsworth 1999).

## **Data**

### *Micro-fractured grains*

Micro-fractured sand grains are observed in all sandstone intrusions examined from the TGIC (late Eocene, Zvirtes et al. 2020) and the PGIC (Danian) and are previously described from sandstone intrusions in the Santa Cruz Mudstone (Miocene, Scott et al. 2009). All sand grains are texturally immature (angular to sub-angular) in fine- to fine to medium grained, poorly sorted sandstone. Poor consolidation is characteristic, samples typically possible to crush under finger pressure.

*Thin sections.* Open and closed fractures are identified in thin sections. In both the TGIC and PGIC, quartz has planar, arcuate and irregular fractures (Fig. 1a & c). Micro-fractures in feldspar in the TGIC follow cleavage and twin plans (Fig. 1b), and micro-fractures in feldspar in the PGIC are predominantly similar to those in quartz with occasional faint (hairline) micro-fractures following cleavage (Fig. 1d). Micro-fractures in lithic fragments are difficult to discern although chert grains are similar to quartz in the TGIC (Fig. 1a). Silt-sized grains are common and micro-fractures are present. Fractures terminate at grain boundaries and adjacent grains do not share common fracture orientation. Jigsaw grain geometry (*sensu* Duranti & Hurst 2004) is present where individual grains are partially disintegrated (Fig. 1d). Parent units in the TGIC have <10% micro-fractured grains whereas sandstone intrusions that emanate from them have up to ~30% micro-fractured grains (Zvirtes et al. 2020).

*BSEM.* Closed fractures are not detected and only PGIC data are presented. Quartz and feldspar grains have similar irregular and arcuate micro-fractures in angular texturally immature grains (Fig. 2a). A few faint hairline fractures are present on some feldspar grains. Intensity of micro-fractures in individual grains varies greatly, for example in quartz grains  $q_1$ ,  $q_2$  and  $q_3$  (Fig.2b) where  $q_1$  is broken into discrete parts,  $q_2$  is intensely micro-fractured but retains a distinct grain margin, and  $q_3$  is so



intensely micro-fractured that distinct grain margins are difficult to define. The constituent fragments of **q<sub>3</sub>** retain diverse fracture characteristics including, sharp arcuate and  $\mu\text{m}$ -scale serrate (white arrows) margins. Jigsaw textures are common but rarely match perfectly across fractures, because of  $\mu\text{m}$ -scale grain rotation during fracturing. All fractures terminate at the margins of individual grains. Fracture aperture may exceed 10  $\mu\text{m}$  but apertures taper and often do not transect entire grains (Fig. 2, **f<sub>1</sub>**, **q<sub>4</sub>**; Fig. 3a, **b**). The uppermost fracture in **f<sub>1</sub>** has *en echelon* fracturing toward its tip. Silt-sized particles form two large areas of the field of view (Fig. 2, **si**) in which individual grains are angular, disorganized and associated with large (>50  $\mu\text{m}$ ) pores. Some grains are micro-fractured including jigsaw textures but generally the margins of adjacent grains do not match.

Change in geometry and orientation within individual and adjacent fractures is common (Fig. 3). In Fig. 3 the largest grain “**a**” has a large penetrative fracture that tapers and near the top of the image intersects concentric hairline fractures. In the bottom left area of the image is a zone of concentric hairline fractures. Along the base of grain “**a**,” two slit-sized slivers (white arrows) are partially detached from the host along matching cusped fracture surfaces and translated to the left. Grain “**b**” has a single main tapering fracture with low curvature margins; the upper margin has irregular  $\mu\text{m}$ -scale relief. The rest of grain “**b**” has an irregular polygonal network of fractures of varying intensity and aperture. Grain “**c**” has a “sawtooth” fracture with clearly defined hackles, at least three smaller perpendicular fractures, and several faint arcuate hairline fractures. Grain margins are predominantly fracture planes. There is no evidence of grain or fracture alignment in individual grains nor in adjacent grains (Figs. 2 & 3).

*SEM.* Closed fractures are not detected. Quartz and feldspar grains have fractured surfaces and arcuate, planar and irregular micro-fractures. Open micro-fractures are pervasive, some of which are up to  $\sim 10$   $\mu\text{m}$  across with jigsaw geometry and  $\mu\text{m}$ -scale hackles (Fig. 4a). Preferred fracture orientation is not noted although fractures in the top part of the image are shorter and lower aperture. Silt-sized feldspar (Fig. 4b) has generally arcuate tapering fractures and exhibits a rich variety of surface textures, the most prominent of which are arrays of sub- $\mu\text{m}$  scale hackles.

*MCT.* A 3D data volume is derived, and only open fractures are detected. Slices through the 3D volume create infinitely thin density images like BSEM but with lower resolution. Pale grey-tone areas approximate to grains with poor sorting and little obvious alignment (Fig. 5a). Several grains have dark (low density) areas that are open fractures. Extraction of individual grains allows rotation of the grain image and reveals tapering, arcuate fractures (Fig. 5B).

Table 1 summaries key characteristics of the micro-fractures observed in Figs. 1 to 6.

#### *Mudstone clasts*

Mudstone clasts are very common in sandstone intrusions and occur in sizes from sand grade to many 10's m across. Images of petrographic thin sections and BSEM from the Santa Cruz Mudstone (late Miocene) are modified from Scott et al. (2009). Mudstone clasts are readily identified in thin section by colour (black), have open micro-fractures (white arrows), and in this example occur among micro-fractured quartz grains (Fig. 6a). Mudstone clasts are on average slightly coarser than the average grain size of the framework grains. Mudstone clasts are sometimes so abundant that they form  $\sim 40\%$  of content by volume and form an extremely low-

density matrix for the framework grains, some of which are micro-fractured (Fig. 6b). Large mudstone clasts are locally common and have micro-fractures propped open by angular sand and silt grains, an example of which is ~3 mm long, up to at least 2mm aperture and tapers away from the mudstone clast margin (Fig. 7a and 7b*i*). Smaller (<1 mm) indentations propped by sand and silt are incipient fractures (Fig. 7b*ii*). In the centre of the mudstone, several isolated sand grains occur embedded in the mudstone, a group of which form a linear trend (Fig. 7a). The upper left and lower right clast margins are diffuse mixtures of mud and sand grains (Fig. 7a & 7b*iv*). Gradations of mud and sand are not present. Other grain margins are sharp with limited mixing of mud and sand (Fig. 7a & 7b*v*).

#### *Heavy minerals*

Possible variations in relative mineral hardness on mineral durability (Fig. 7) and the role of mineral density contrasts on hydrodynamic fractionation during sand injection are derived from data in Hurst et al. (2017). Evaluation of relative hardness utilises the ratio of apatite and tourmaline, which have similar specific gravity, 3.16 to 3.22 gcm<sup>-3</sup> and 2.82 to 3.32 gcm<sup>-3</sup>, respectively, but apatite is markedly less hard than tourmaline, 5 and 7 to 7.5, respectively (Fig. 7b). When co-occurring in a flow the ratio of apatite to tourmaline (ATi) decreases with the duration of abrasion and grain breakage. A clear trend of increasing ATi upward is present in the parent units (ATi values 45 to 59) into the injection complex, with the lowest values (26 to 48) near the top of the PGIC (Fig. 8a). Preservation of apatite is sensitive to interaction with meteoric water (Bramlette, 1941; Hurst & Morton, 2014) and petrographic analysis reveals no indication of apatite dissolution. Exceptions to this are the two very low ATi's present in the central part of the Tierra Loma Member (Fig. 8a) caused by post-depositional deep weathering that almost completely dissolution of apatite (Hurst et

al. 2017). Other common heavy minerals susceptible to dissolution during weathering, such as titanite, are similarly depleted (Fig. 3 in Hurst et al. 2017).

Ratios of mechanically ultra-resistant minerals zircon and tourmaline (ZTi) are used to evaluate the effects of hydrodynamic fractionation of heavy minerals during injection. Although similar mechanically, zircon and tourmaline lie at opposite ends of the heavy-mineral density range (zircon 4.6 to 4.7 g cm<sup>-3</sup>; tourmaline 3.06 g cm<sup>-3</sup>) and are expected to density-fractionate during upward fluid flow. A gradual increase in ZTi upward is recorded (Fig. 9) with relatively uniform ZTi near the base (Fig. 9, T, U, V) and the high values in the shallowest high-angle dykes (Fig. 9, GG, E).

## Discussion

Both the PGIC and TGIC have multiple km-scale exposures of entire sections through intrusive complexes and their parent units thus obviating many of the limitations when working with smaller outcrops or less well-exposed outcrop. Host strata and intrusions are poorly consolidated, which eases sampling and avoids sample damage and possible introduction of artefact features when preparing samples for analysis. Both the PGIC and TGIC have  $T_{\max}$  in the range ~40-50°C to <60°C based on clay mineralogy, and the co-occurrence of opal A and opal CT (Bjørlykke 2010). Organic maturation indices fail to constrain  $T_{\max}$  in this temperature range. Using vitrinite reflectance data from mudstone and apatite fission track analyses from sandstone, 1.3 to 1.6 km maximum burial is estimated for the Santa Cruz Mudstone (Thompson et al. 1999), which is consistent with co-existing silica polymorphs in the same section that suggest maximum burial depth of 1 to 2 km (El Sabbagh and Garrison, 1990). The burial depths are consistent with values of  $T_{\max}$  estimated for the PGIC and TGIC. Evidence of silicate diagenesis in sandstone

intrusions from PGIC, TGIC and the Santa Cruz Mudstone is absent or very minor (Scott et al. 2009; Scott et al. 2013; Zvirtes et al. 2020).

Features described herein are all from sandstone intrusions in giant injection complexes and although scale-independence of intrusion geometry is recognised (Hurst et al. 2003) it is not known whether similar presence and intensity of micro-fracturing occurs in smaller sand intrusions, some of which may be cm-scale (Fig. 5c, Wilkins et al. 2018).

#### *Geometry and origin of micro-fractures*

Micro-fractured grains are associated with shock metamorphism at very high T/P conditions (Stöffler & Langenhorst 1994; Kenkmann et al. 2014), which is a widely used diagnostic for inferring meteorite impact (Bunch & Cohen 1964). Mechanical processes produce micro-fractured grains during metamorphism typically along fracture planes (Wenk et al. 2011) and burial diagenesis that may include formation of deformation bands (Chuhan et al. 2002; Storvoll & Bjørlykke 2004). Shock metamorphism of quartz produces compressional and shear deformation within grains (Trepmann 2008), planar deformation features related to fracture along cleavage planes (Ferrière et al. 2009) and feather lamellae that cross-cut cleavage (Poelchau & Kenkmann 2011). Mechanical processes associated with metamorphism or burial diagenesis tend to align grains with sub-parallel inter-granular fractures, and the in case of deformation bands, tightly packed grains are juxtaposed adjacent to less consolidated grains. No similar features to these occur in samples described herein (Table 1).

Arcuate fractures typify most micro-fractured grains (Table 1) either as single fractures or as linked series of fractures. In reality, apparent planar fractures are low-

curvature arcuate fractures (Figs 1c (bottom centre grain) & 3 b). Fractures bifurcate, crosscut, taper, interfere, form polygonal patterns (often hairline) and may be so intense that individual grains have the appearance of agglomerations of finer grains (Fig. 2  $q_2$  and  $q_3$ ). Individual grains preserve evidence of multiple fracture events such as the top area of grain **a** (Fig. 3), where curved hairline fractures are cut and displaced by a large fracture. On the same grain (bottom right) curved hairline fractures are well-preserved but have highly irregular sub- $\mu\text{m}$  fracture surfaces; where the curved hairline fracture reaches the grain margin, a  $\mu\text{m}$ -scale displacement occurs (circled on Fig. 3). Fractures stop at grain margins, fracture intensity varies between adjacent grains, and fractures in adjacent grains lack common orientation (Table 1, Figs 2 & 3). Similar micro-fractured grains occur in columnar sandstone intrusions from Kodachrome Basin (fig. 10D, also F and G but lower resolution, Ross et al. (2014) although not referred to in the paper).

Micro-scale hackles are common on small fracture surfaces (Price & Cosgrove 1990) and examples herein are no exception although matching hackles on opposing fracture margins are uncommon (Fig. 3 c). Larger than  $\mu\text{m}$ -scale hackles and sub- $\mu\text{m}$  scale hackles are present on the fractured surface of a silt-sized feldspar (Fig. 4b). Together with preservation of numerous angular irregularities and displaced grain-slivers (Fig. 3), prevailing fresh fracture surfaces are evidence of minimal grain abrasion, or when present inherited features formed during deposition of parent units.

Exceptions to the development of arcuate micro-fractures follow cleavage planes in feldspar (Fig. 1) in the TGIC (Zvirtes et al. 2020). The cleavage fractures are iron-oxide stained, which in this case is attributed to alteration associated with erosion of deeply weathered Sierran source terrane formed during the Palaeocene-Eocene

thermal maximum (Kennett & Stott 1991). Similar iron stained fractures do not occur in quartz and chert grains. Weathering of the feldspar exploited and weakened the cleavage planes making them more prone to failure than if they were derived from less intensely weathered terrane in which` arcuate fractures predominate (Figs 1c, 2a).

#### *Generation and timing of micro-fractures*

Micro-fracture of grains is fundamental to larger-scale brittle failure of rock (Hallbauer et al. 1973; Kranz 1983). In sandstone intrusions the lack of inter-granular micro-fracture arrays (Figs 1, 2 & 3 and Table 1, 5, 6 & 7) shows that fracture generation and propagation in individual or adjacent grains were not responding to focused mechanical stress that would lead to formation of macro-scale brittle failure (Reches & Lockner 1994; Healy et al. 2006). There is no evidence that the micro-fractures post-date sand injection (Table 1). Individual grains reveal evidence of multiple phases of fracture, as exemplified in Fig. 3, where the largest grain (**a**) records at least three phases of fracture; two grain margin locations have concentric hairline fractures, together with a tapering trans-granular fracture. The large fracture displaces and deforms the hairline radial fractures in the top area of the grain, so must post-date it. Temporal relationships with the radial hairline fractures on the bottom right of the grain cannot be established but the spatial relationship suggests an unrelated phase of fracture. All three areas of fracture formed by impact stress exerted on grains from different directions, and probably at different times.

Duration of emplacement of a giant sand injection complex is believed to take several days (Hurst et al. 2011) with shorter individual pulses of flow predominating in intrusions more than a few centimetres in width (for example, Scott et al. 2009).

Constraint of duration is however problematic and directly relevant analogues are elusive and invariably associated with major earthquakes, which by contrast with ancient giant injection complexes (Huuse et al. 2004; Vigorito et al. 2008; Vigorito & Hurst 2010; Zvirtes et al. 2019) involve liquefaction and fluidisation of shallow-buried (meters) parent units (Obermeier 1998). Observation of major sand extrusion is restricted to oral historical accounts of terrestrial origin (Obermeier 1989). Estimates of average flow velocity vary substantially (Duranti 2007; Hurst et al. 2011) and the range of velocity of individual grains is unknown, although corrasion (Fig. 7 and Scott et al. 2009) requires substantially higher velocity than estimates of average flow velocity. Widespread occurrence of intense grain micro-fracture (Scott et al. 2009; Luzinski et al. 2019; Zvirtes et al. 2020) further supports high velocity intergranular collisions.

These conditions are fundamentally different than experimental conditions in which symmetrical cone cracks form by Hertzian loading of isotropic materials under uniaxial stress (Lawn 1998) although the concentric hairline cracks are visually similar. Micro-fracture geometry formed under uniaxial stress in experiments is steered by the trigonal symmetry of quartz (Timms et al. 2010), but in sandstone intrusions the inter-granular textures (Fig. 2) and micro-fractures in grains (Figs 3 & 4) are not obviously related to crystal symmetry. Rather, multiple collisions between grains in many different orientations relative to their internal crystallographic symmetry, have predominantly fractured surfaces (Fig. 4b) with intra-granular fractures with visually random orientation (Table 1, Figs 2a & 3). The available petrographic evidence together with the absence of observations to support post-fluidisation generation of micro-fractures supports interpretation of micro-fracturing as being a characteristic of large-scale sand fluidisation. Petrographic data from the



TGIC, confirm that parent units that have <10% micro-fractured grains whereas sandstone intrusions associated with them have up to ~30% micro-fractured grains (Zvirtes *et al.* 2020).

### *Abrasion versus fracturing*

Predominantly angular framework grains characterise sandstone intrusions from the PGIC, TGIC and Santa Cruz Mudstone (Figs 1, 2 & 6) with fracture surfaces predominant (Figs 3 & 4). Subordinate sub-rounded grains and facets occur (<2% of grains, Figs 1 & 6). Angular silt-sized quartz and feldspar is common in all samples, locally representing 20-30% of the grain content (Figs 2, 4b & 6a) and derived from breakage of coarser sand grains during injection (Figs 2, 3 & 4a). Similarity between intensely fractured grains (Fig. 2a **q<sub>1</sub>**, **q<sub>2</sub>** & **q<sub>3</sub>**) and areas of silt-sized grains (Fig. 2a **si**) is suggestive that intense micro-fracturing is the precursor to silt particles. Irregular grain margins observed petrographically (Figs 1c, d) and using BSEM (Figs. 2 & 3), are fracture surfaces, including hackles, when viewed using SEM (Fig. 4b). Presence of abraded surfaces on framework grains in the PGIC is minor, and when present they terminate against fracture surfaces (Luzinski *et al.* 2019) thus their formation pre-dates fracturing.

Despite many heavy minerals being relatively less hard than quartz and feldspar (Fig. 8b), they undergo insignificant modification by abrasion in a large modern drainage basin with ~2200 km transport distance followed by at least 1000 km of longshore coastal and aeolian transport (Garzanti *et al.* 2012). Reduced abundance of apatite, in the absence of evidence for diagenetic dissolution, relative to harder but similarly dense tourmaline in the PGIC (Fig. 8a) is contrary to this. More vigorous abrasion occurred during the short period of sand injection than from prolonged

depositional processes. Mechanical diminution of apatite is known during borehole drilling with polycrystalline diamond cutter (PDC) drill bits (Morton et al. 2010). Herein it is inferred that the energy of inter-granular collisions that cause mechanical diminution of apatite during sand injection are similar to those between apatite and framework grains during PDC drilling, very high grain velocity is probable. Abrasion and fracture of zircon in the PGIC, the hardest commonly occurring heavy mineral (Fig. 8b), is further independent evidence of high grain velocity during sand injection (Luzinski et al. 2019). Collisions between zircons are extremely unlikely during sand injection as zircon accounts for a fraction of a percent in the whole rock mineralogy. As recorded independently (Bouroullec & Pyles 2010) angular to sub-angular grains in sandstone intrusions, which combined with evidence of inter-granular collisions and grain micro-fracture supports intense, short-duration flow during which grain-breakage and comminution occurred but with minimal abrasion between similarly hard grains.

*Embedding of sand grains in mudstone: corrasion*

Mudstone clasts are common in sandstone intrusions (Kawakami & Kawamura 2002; Hurst et al. 2003; Hurst et al. 2011) with clasts of pebble, cobble and coarser, as well as sand-grade grains. When coarse mudstone clasts are abundant in a sand-supported matrix they form mudstone clast breccia (also termed injection breccia), a characteristic facies of sand injectites common in borehole core (Purvis et al. 2003; Duranti & Hurst 2004; De Boer et al. 2007). Variable clast rounding occurs, typically over restricted sections of clast or grain margins (Duranti & Hurst 2004; DeBoer et al. 2007; Zvirtes et al. 2019). Petrography confirms that similar micro-scale features occur (Fig. 7), which are interpreted to form by corrasion and are diagnostic of high granular velocity (Scott et al. 2009).

Armouring by sand grains on the surfaces of mud clasts was first described from a range of fluvial environments and is associated with sand encrustation by the rolling of rounded balls of mud over loose sand (Bell 1940; Picard & High 1973). Mud balls are typically 0.05 to 0.3 m diameter (Bell 1940; Diffendal 1984) and occur in coarse-grained fills of erosional scours or troughs (Little 1982; Diffendal 1984). Similar encrusted mudstone clasts are recorded from other sedimentary environments, including deep-water depositional systems (Kuenen & Migliorini 1950). In deep-water environments armouring of mudstone clasts may occur by rolling in loose sand but may also occur if clasts are suspended within a turbulent flow. In both cases the armouring by sand makes the mudstone clast less susceptible to mechanical decomposition (Fonnesu et al. 2018).

In detail, individual small mudstone clasts have sand-propped micro-fractures (Fig. 7i & ii) and isolated individual sand grains within mudstone clasts (Fig. 7iii). Isolated sand grains may partially prop micro-fractures, be part of oblique sections through propped fractures that elsewhere have more sand grains or may be isolated grains that penetrated the mudstone in the absence of micro-fractures. These cannot be differentiated petrographically but the first two require hydraulic fracturing, and the last requires that sand grains impact mudstone surfaces at non-zero angles and thereby detach particles from the surfaces, the process of corrasion (Allen 1984). In all cases turbulent high-velocity flow is inferred (Scott et al. 2009; Hurst et al. 2011; Luzinski et al. 2019). Short, incipient micro-fractures (Fig. 7 ii) are the early stages of micro-fracture propagation. Embedding of sand grains deep within individual mudstone clasts records progressive decomposition of the mudstone clast, entirely contrary behaviour to that described by armouring or encrusting of mudstone clasts in turbiditic environments (Fonnesu et al. 2018).

At least equally significant in terms of differentiating the association between embedding and encrusting by sand grains, are the margins of mudstone clasts. For approximately half the length of the clast boundary the margin is a diffuse mix of sand and mud (Fig. 7iv). This coincides with the locations of micro-fractures. The diffuse mix is extremely unlikely to form by rolling of a mudstone clast in loose sand. Other margins have abrupt transitions from mud to sand (Fig. 7v). Sandstone in Fig. 7 is independently interpreted as a sandstone intrusion (Thompson et al. 1999). Interpretation of the micro-fractures and the diffuse clast boundaries is attributed to hydraulic fracturing of the mudstone and spontaneous injection of fluidised sand.

Although mudstone clasts in sandstone intrusions are derived from hydraulic fracturing of mudstone-rich strata, it cannot be proven with petrographic data whether micro-fractures propped open by sand grains exploited pre-existing hydraulic fractures. Sand propped micro-scale fractures in mudstone clasts and embedded sand grains, as distinct from armoured or encrusted mudstone clasts, may be diagnostic of sandstone intrusions. Comparison with relevant petrographic data from similar clasts in depositional environments is required to verify this claim.

#### *Hydrodynamic fractionation*

The ratio of zircon to tourmaline (ZTi) is a robust index of hydrodynamic fractionation (Morton & Hallsworth 1999) as both minerals are ultra-stable chemically and mechanically but lie at opposite ends of the heavy mineral density scale (zircon 4.6 to 4.7 g cm<sup>-3</sup>, tourmaline 2.82 to 3.32 gcm<sup>-3</sup>). As fluidised sand rises through an injection complex, zircon the denser mineral, tends to fall out of suspension whereas tourmaline will tend to stay in suspension. Consequently, moving upward in an

injection complex one should expect ZTi to rise, which is what is recorded (Fig. 9a). Discussion of the significance of heavy mineral ratios should be tempered by the absence of relevant analogue data with which to make comparison. Sampling in Moreno Gulch was done primarily to investigate provenance relationships between sandstone parent units in the Uhalde and Dosados sandstones and the PGIC (Hurst et al. 2017). Effects of hydrodynamic segregation were secondary considerations and the focus of on-going research.

Intrusions (Fig. 9b) in the lower dyke zone (LDZ, samples T, U, V), sill zone (SZ, samples Z, L, K) and upper dyke zone (UDZ, samples H, GG, E) have significant variation in ZTi associated with hydrodynamic segregation during sand injection. Most obviously the sill zone (SZ) has lower ZTi than present in LDZ or UDZ, and the UDZ has the highest ZTi values. As already noted, a ZTi increase upward is expected as zircon will segregate relative to tourmaline in a vertical flow. In the approximately 550 m from the top of the Dosados Sandstone to location of sample E Zti increases from <75 to >90, a significant increase in zircon coming out of suspension. Lower values (ZTi ~60) in SZ suggest that less hydraulic segregation occurred, which in terms of the geometry of the intrusions coincides with sand emplacement at low angles to bedding. Individual sills and other low-angle intrusions in the PGIC are typically <10 m thick. ZTi does not indicate volumes of zircon and tourmaline present only their relative abundance. Because both minerals are physically and chemically ultra-stable, their concentrations are very unlikely to be affected by other variables.

Sill zones are where the main hydrocarbon reservoirs in sand injection complexes occur (Duranti et al. 2002; Schwab et al. 2014; Hurst & Vigorito 2017; Skjaerpe et al. 2018; Satur et al. 2020; Pelletier & Gunn, *in press*) and if lower ZTi values are

characteristically lower than dykes, this may aid distinction between subsurface dykes and sills even when core is unavailable. If relationships between ZTi and location in a subsurface vertical section in an injection complex are established, it may support estimation of depth to parent units and thickness of injection complexes. Hydraulic fractionation of zircon, or other dense minerals, in dykes could in a vertical section, be misinterpreted as a gradual change in heavy mineral provenance, a hypothesis that requires testing by independent chemical analysis of common varietal heavy mineral species such as garnet, tourmaline, apatite, rutile and titanite (Hurst & Morton 2014; Morton et al. 2014; Hurst et al. 2017).

## **Conclusion**

In giant injection complexes petrographic and mineralogical data are of diagnostic value. Grain micro-fracture and corrosion record that sand injection had high energy and velocity grain collisions in inferred dilute granular suspensions. During the vertical flow of sand heavy mineral assemblages show the susceptibility of apatite to abrasion and the density segregation of zircon, both may be characteristics of giant sand injection complexes.

Micro-fractures in sandstone intrusions are texturally distinct compared with those formed by shock metamorphism, faulting or formation of deformation bands. Micro-fractured quartz and feldspar record high energy collisions between sand grains during sand injection. Locally up to 60% of the total grains present are micro-fractured. Grain surfaces are pervasively fractured and create texturally immature sandstone, which is poorly sorted often with significant content of silt-sized framework grains that formed by inter-granular collisions. Adjacent grains do not share common orientation of fractures and grain packing is irregular. Sand grains

record fracturing from several spatially and temporally distinct collisions. All fractures terminate at grain margins. Collectively these characteristics are diagnostic of sandstone intrusions.

Sand grains embedded in mudstone clasts form by corrasion when high velocity fluidised grains impact the mudstone at non-zero angles and penetrate their interior.

These are texturally distinct from surface encrustation or armouring of mudstone clasts known from depositional environments.

Heavy mineral assemblages that are otherwise mineralogically and chemically similar, preserve evidence of less persistence of apatite upward relative to harder but similarly dense tourmaline (ATi), susceptibility to abrasion is inferred. In the same section, hydrodynamic segregation of zircon and tourmaline (ZTi) occurs. Zircon is the denser of these ultra-stable heavy minerals and moving up through the injection complex becomes progressively more concentrated within sandstone dykes relative to tourmaline. Changes of ATi and ZTi in depositional environments are provenance indicators whereas in an injection complex they record a process.

## References

ALLEN, J.R.L. 1984. *Sedimentary Structures: Their Character and Physical Basis*. Elsevier, Amsterdam, 663 p.

BARTOW, J.A. 1991. Cenozoic Evolution of the San Joaquin Valley, California. US Geological Survey Professional Paper, 1–40.

BARTOW, J.A. & NILSEN, T. 1990. Review of the Great Valley Sequence, Eastern Diablo Range and Northern San Joaquin Valley, Central California. US Geological Survey Professional Papers, **25**.

BELL, H. S. 1940, Armored mud balls: their origin, properties, and role in sedimentation. *Journal of Geology*, **48**, 1-31.

**BJØRLYKKE, K. 2010. Shales, silica deposits and evaporites. Ch. 5, In: BJØRLYKKE, K. (ed) *Petroleum Geoscience: From sedimentary environments to rock physics*. Springer Verlag, Chapter 5, 201-212.**

BOEHM, A. & MOORE, C.J., 2002, Fluidized sandstone intrusions as an indicator of Paleostress orientation, Santa Cruz, California: *Geofluids*, **2**, 147–161.

**BOUROLLEC, R. & PYLES, D.R. 2010. Sandstone Extrusions and Slope Channel Architecture and Evolution: Mio-Pliocene Monterey and Capistrano Formations, Dana Point Harbor, Orange County, California, U.S.A. *Journal of Sedimentary Research*, **80**, 376-392.**

BRAMLETTE, M.N. 1941. The stability of minerals in sandstone. *Journal of Sedimentary Petrology*, **11**, 32-36.

BRIEDIS, N.A., BERGSLIEN, D., HJELLBAKK, A., HILL, R.E. & MOIR, G.J. 2007. Recognition criteria, significance to field performance, and reservoir modeling of sand injections in the Balder Field, North Sea. In: HURST, A. & CARTWRIGHT, J. (eds), *Sand injectites: implications for hydrocarbon exploration and production*, American Association of Petroleum Geologists Memoir **87**, Tulsa, pp. 91–102.

BUNCH, T.E. & COHEN, A.J. 1964. Shock deformation of quartz from two meteorite craters. *Geological Society of America Bulletin*, **75**, 1263-1266.

CHUHAN, F.A., KJELDSTAD, A., BJØRLYKKE, K. & HOEG, K. 2002. Porosity loss in sand by grain crushing – experimental evidence and relevance to reservoir quality. *Marine and Petroleum Geology*, **19**, 39–53.

De BOER, W., RAWLINSON, P.B. & HURST, A. 2007. Successful exploration of a sand injectite complex: Hamsun prospect, Norway Block 24/9. In: HURST, A. & CARTWRIGHT, J. (eds) *Sand Injectites: Implications for Hydrocarbon Exploration and Production*. American Association of Petroleum Geologists, Memoir **87**, 65-68.

DIBLEE, T.W., Jr. 2007. Geological map of the Chounet Ranch Quadrangle, Fresno County, California. In: MINCH, J.-A. (ed) Dibblee Geology Centre Map, DF-**321**.

DIETZ, V. 1973. Experiments on the influence of transport on shape and roundness of heavy minerals. *Contributions to Sedimentology*, **1**, 103–125.



DIFFENDAL, R.F. 1984. Armored mud balls and friable sand megaclasts from a complex early Pleistocene alluvial fill, southwestern Morrill County, Nebraska. *Journal of Geology*, **92**, 325-330.

DIXON, R.J., SCHOFIELD, K., ANDERTON, R., REYNOLDS, A.D., ALEXANDER, R.W.S., WILLIAMS, M.C. & DAVIES, K.G. 1995. Sandstone diapirism and clastic intrusion in the Tertiary submarine fans of the Bruce–Beryl Embayment, Quadrant 9, UKCS. *In*: HARTLEY, A.J. & PROSSER, D.J. (eds) *Characterisation of Deep-Marine Clastic Systems*, Geological Society of London, Special Publication **94**, 77–94.

DURANTI, D. 2007. Large-scale sand injection in the Paleogene of the North Sea: modeling of energy and flow velocities. *In*: HURST, A. & CARTWRIGHT, J. (eds) *Sand Injectites: Implications for Hydrocarbon Exploration and Production*. American Association of Petroleum Geologists, Memoir **87**, 129–139.

DURANTI, D. & HURST, A. 2004. Fluidization and injection in the deep-water sandstones of the Eocene Alba Formation (UK North Sea). *Sedimentology*, **51**, 1–27.

DURANTI, D., HURST, A., BELL, C. & GROVES, S. 2002. Injected and remobilised sands of the Alba Field (UKCS): sedimentary facies characteristics and wireline log responses. *Petroleum Geoscience*, **8**, 99-107.

EL-SABBAGH, D. & GARRISON, R.E. 1990. Silica diagenesis in the Santa Cruz mudstone (upper Miocene), La Honda Basin, California. *In*: GREENE, H. G., WEBER, G.E., WRIGHT, T.L. & GARRISON, R.E. (eds) *Geology and Tectonics of the Central California Coastal Region, San Francisco to Monterey*, American Association of Petroleum Geologists, Bakersfield, California. vol. **67**, p. 123–132.

FERRIÈRE, L., MORROW, J.R., AMGAA, T. & KOEBERL, C. 2009. Systematic study of universal-stage measurements of planar deformation features in shocked quartz: implications for statistical significance and representation of results. *Meteoritics & Planetary Science*, **44**, 925-940.

FONNESU, M., FELLETTI, F., HAUGHTON, P.D.W., PATACCI, M. & McCAFFREY, W.D. 2018. Hybrid event bed character and processes linked to turbidite system sub-environments: the North Apennine Gottero Sandstone (north-west Italy). *Sedimentology*, **65**, 151-190. ISSN 0037-0746 <https://doi.org/10.1111/sed.12376>

GARZANTI, E., ANDO, S. & VEZZOLI, G. 2008. Settling equivalence of detrital minerals and grain-size dependence of sediment composition. *Earth and Planetary Science Letters*, **273**, 138-151.

GARZANTI, E., ANDO, S., VEZZOLI, G., LUSTRINO, M., BONI, M. & VERMEESCH, P. 2012. Petrology of the Namib Sand Sea: long-distance transport and compositional variability in the wind-displaced Orange Delta. *Earth-Science Reviews*, **112**, 173-189.

GRIPPA, A., HURST, A. PALLADINO, G., IACOPINI, D. LECOMTE, I. & HUUSE, M. 2019. Seismic imaging of complex geometry: forward modelling of sandstone intrusions. *Earth and Planetary Science Letters*, **513**, 51-63.

HALLBAUER, D. K., WAGNER, H. & COOK, N. G. W. 1973. Some observations concerning the microscopic and mechanical behaviour of quartzite specimens in stiff, triaxial compression tests, *Int. J. Rock Mech. Min. Sci. Geomech. Abstr.*, **10**, 713–726.

HEALY, D., JONES, R. R. & HOLDSWORTH, R. E. 2006. Three-dimensional brittle shear fracturing by tensile crack interaction, *Nature*, **439**, 64–67

HURST, A., CARTWRIGHT, J.A. & DURANTI, D. 2003. Fluidisation structures in sandstone produced by upward injection through a sealing lithology. In:(VAN RENSBERGEN, P., HILLIS, R.R., MALTMAN, A.J. & MORLEY, C.K. (eds), *Subsurface sediment mobilization*. Geological Society, London, Special Publications, **216**, 123-137.

HURST, A., CARTWRIGHT, J.A., HUUSE, M. & DURANTI, D. 2006. Extrusive sandstones (extrudites): a new class of stratigraphic trap? In: ALLEN, M.R., GOFFEY, G.P., MORGAN, R.K. & WALKER, I.M. (eds), *The Deliberate Search for the Stratigraphic Trap*, Special Publication, **254**. Geological Society, London, pp. 289–300.

HURST, A. & MORTON, A.C. 1988. An application of heavy-mineral analysis to lithostratigraphy and reservoir modelling in the Oseberg Field, northern North Sea. *Marine and Petroleum Geology*, **5**, 157-170.

HURST, A. & MORTON, A.C. 2014. Provenance models: the role of sandstone mineral-chemical stratigraphy. In: SCOTT, R.A., SMYTH, H.R., MORTON, A.C. & RICHARDSN, N. (eds) *Sediment Provenance Studies in Hydrocarbon Exploration and Production*. Geological Society of London, Special Publication **386**, 7-26.

HURST, A., MORTON, A.C., SCOTT, A., VIGORITO, M. & FREI, D. 2017. Heavy-mineral assemblages in sandstone intrusions: Panoche Giant Injection Complex, California, USA. *Journal of Sedimentary Research*, **87**, 1-18 (online DOI: <http://dx.doi.org/10.2110/jsr.2017.22>)

HURST, A., SCOTT, A. & VIGORITO, M. 2011. Physical characteristics of sand injectites. *Earth-Science Reviews*, **106**, 215-246.

HURST, A. & VIGORITO, M. 2017. Saucer-shaped sandstone intrusions: an underplayed reservoir target. *American Association of Petroleum Geologists Bulletin*, **101**, 625-633.

HUUSE, M., DURANTI, D., STEINSLAND, N., GUARGENA, C.G., PRAT, P., HOLM, K., CARTWRIGHT, J.A. & HURST, A., 2004. Seismic characteristics of large-scale sandstones intrusions in the Paleogene of the South Viking Graben, UK and Norwegian North Sea. *In*: DAVIES, R.J., CARTWRIGHT, J.A., STEWART, S.A., LAPPIN, M. & UNDERHILL, J.R. (eds) *Seismic technology: Application to the Exploration of Sedimentary basins*. Geological Society, London Memoir, **29**, 263–277.

INGERSOLL, R.V. 1979. Evolution of the Late Cretaceous forearc basin, northern and central California. *Geological Society of America Bulletin*, **90**, 813–826.

KAWAKAMI, G. & KAWAMURA, M. 2002. Sediment flow and deformation (SFD) layers: evidence for intrastratal flow in laminated muddy sediments of the Triassic Osawa Formation, northeast Japan. *Journal of Sedimentary Research*, **72**, 171–181.

KENNETT, J.P. & STOTT, L.D. 1991. Abrupt deep-sea warming, palaeoceanographic changes and benthic extinctions at the end of the Palaeocene. *Nature*, **353**, 225-229.

KENKMANN, T., POELCHAU, M.H. & WULF, G. 2014. Structural geology of impact craters. *Journal of Structural Geology*, **62**, 156-182.

KOMAR, P.D. 2007. The entrainment, transport and sorting of heavy minerals by waves and currents. *In*: MANGE, M.A. & WRIGHT, D.T. (eds) *Heavy Minerals in Use*, Elsevier, Amsterdam, *Developments in Sedimentology*, **58**, p. 3–48.

KRANZ, R. L. 1983. Microcracks in rocks: A review, *Tectonophysics*, **100**, 449–480.

KUENEN, PH. H. & MIGLIORINI, C.I. 1950. Turbidity currents as a cause of graded bedding. *Journal of Geology*, **58**, 91-127.

LAWN, B.R. 1998. Indentation of Ceramics with Spheres: a century after Hertz. *Journal of American Ceramic Society*, **81**, 1977-1991.

LITTLE, R, D. 1982. Lithified armored mud balls of the Lower Jurassic Turners Falls Sandstone, north-central Massachusetts. *Journal of Geology*, **90**, 203-207.

LONERGAN, L.J., BORLANDELLI, C., TAYLOR, A., QUINE, M. & FLANAGAN, K. 2007. The three-dimensional geometry of sandstone injection complexes in the Gryphon Field, United Kingdom, North Sea. *In*: HURST, A. & CARTWRIGHT, J. (eds.) *Sand Injectites*:

*Implications for Hydrocarbon Exploration and Production*. American Association of Petroleum Geologists, Memoir **87**, p. 103–112.

LUZINSKI, W.M., HURST, A. & MORTON, A.C. 2019. Textural development of sand grains in natural fluidisation. *British Sedimentological Research Group*, University of London, Royal Holloway & New College, 13-15 Dec, 2019 (*abstract*).

McGUIRE, D.J. 1988. Stratigraphy, depositional history, and hydrocarbon source-rock potential of the Upper Cretaceous–Lower Tertiary Moreno Formation, Central San Joaquin basin, California. Doctoral thesis, Stanford University, CA.

MANGE, M.A. & MAURER, H.F.W. 1992. *Heavy Minerals in Colour*. Chapman and Hall, London, 147p.

MARGOLIS, S.V. & KRINSLEY, D.H. 1974. Processes of formation and environmental occurrence of microfeatures on detrital quartz grains. *American Journal of Science*, **274**, 449-464.

MORTON, A.C. & HALLSWORTH, C.R. 1999. Processes controlling the composition of heavy mineral assemblages in sandstones. *Sedimentary Geology*, **124**, 3-29.

MORTON, A.C., HALLSWORTH, C.R., KUNKA, J., LAWS, E., PAYNE, S. & WALDER, D. 2010. Heavy mineral stratigraphy of the Clair Group (Devonian) in the Clair Field, west of Shetland, UK. *In*: RATCLIFFE, K.T. & ZAITLIN, B.A. (eds) *Application of Modern Stratigraphic Techniques: Theory and Case Histories*. SEPM, Special Publication, **94**, 183-199.

MORTON, A., McFADYEN, S., HURST, A., PYLE, J. & ROSE, P. 2014. Constraining the origin of reservoirs formed by sandstone intrusions: Insights from heavy mineral studies of the Eocene in the Forties area, U.K. central North Sea. *AAPG Bulletin*, **98**, 54-561.

OBERMEIER, S.F. 1989. The New Madrid Earthquakes: an Engineering-Geologic interpretation of relict liquefaction features. US Geological Survey Professional Paper 1336-B, pp.70.

OBERMEIER, S.F. 1998. Liquefaction evidence for strong earthquakes of Holocene and latest Pleistocene ages in the states of Indiana and Illinois, USA. *Engineering Geology*, **50**, 227–254.

PELLETIER, F. & GUNN, C. (in press). The Gryphon, Maclure, Tullich and Ballindalloch Fields, Blocks 9/18b, 9/18c, 9/19a, 9/23d, 9/24e UK North Sea. *In*: GOFFEY, G. &

GLUYAS, J. G. (eds) *United Kingdom Oil and Gas Fields: 50th Anniversary Commemorative Volume*.

Geological Society, London, Memoirs, **52**, (in press).

PICARD, M. D. & HIGH, L. R. JR. 1973. *Sedimentary Structures of Ephemeral Streams*.

Elsevier, Amsterdam, 223 p.

POELCHAU, M.H. & KENKMANN, T. 2011. Feather features: a low-shock-pressure indicator in quartz. *Journal of Geophysical Research*, 116, B02201, doi:10.1029/2010JB007803, 2011.

PRICE, N.J. & COSGROVE, J.W. 1990. Minor fractures- their nomenclature and ae relationships, Chapter 2, *In: Analysis of Geological Structures*. Cambridge University Press, pp. 42-69.

PURVIS, K., KAO, J., FLANAGAN, K., HENDERSON, J., DURANTI, D., 2002. Complex reservoir geometries in a deep water clastic sequence, Gryphon Field, UKCS: injection structures, geological modelling and reservoir simulation. *Marine and Petroleum Geology*, **19**, 161–179.

RECHES, Z. E. & LOCKNER, D. A. 1994. Nucleation and growth of faults in brittle rocks. *J. Geophys. Res.*, **99**, 18159–18173.

ROSS, J.A., PEAKALL, J. & KEEVIL, G.M. 2014. Facies and flow regimes of sandstone-hosted columnar intrusions: insights from the pipes of Kodachrome Basin State Park. *Sedimentology*, **61**, 1764-1792.

SATUR, N., HURST, A., BANG, A., SKJÆRPE, I. & MUEHLBOECK, S.A. 2020. Characteristics of a wing-like sandstone intrusion, Volund. *In: SILCOCK, S., Huuse, M., Bowman, M., Hurst, A., and Cobain, S., editors, Subsurface Sand Remobilization and Injection Geological Society of London, Special Publication, 493*, <https://doi.org/10.1144/SP493-2017-309>

SCHWAB, A. M., JAMESON, E. W. & TOWNSLEY, A. 2014. Volund Field: development of an Eocene sandstone injection complex, offshore Norway. *In: T. MCKIE, T., Rose, P.T.S., HARTLEY, A.J., Jones, D.W. & Armstrong, T.L. (eds) Tertiary Deep-Marine Reservoirs of the North Sea Region*. Geological Society, London, Special Publications, **403**, 247-260.

SCOTT, A., VIGORITO, M. & HURST, A. 2009. The process of sand injection: internal structures and relationships with host strata (Yellowbank Creek injectite complex, California). *Journal of Sedimentary Research*, **79**, 568-583.

- SCOTT, A., HURST, A. & VIGORITO, M. 2013. Outcrop-based reservoir characterization of a kilometer-scale sand injectite complex. *AAPG Bulletin*, **97**, 309-343.
- SKJÆRPE, I., TØLLEFSEN, I. & ENDRESEN, T. 2018. Developing Viper-Kobra: maximizing recovery by exploiting the unique characteristics of the sand injectite environment. 80th EAGE Conference & Exhibition 2018, 11-14 June 2018, Copenhagen, Denmark, p.3795-3799.
- STORVOLL, V. & BJØRLYKKE, K. 2004. Sonic velocity and grain contact properties in reservoir sandstones. *Petroleum Geoscience*, **10**, 215-226.
- STØFFLER, D. & LANGENHORST, F. 1994. Shock metamorphism of quartz in nature and experiment: I. Basic observation and theory. *Meteorics*, **29**, 155-181.
- THOMPSON, B.J., GARRISON, R.E. & MOORE, C.J. 1999. A late Cenozoic sandstone intrusion west of S. Cruz, California. Fluidized flow of water and hydrocarbon saturated sediments. *In: Garrison, R.E., Aiello, I.W. & Moore, J.C. (eds) Late Cenozoic Fluid Seeps and Tectonics Along the San Gregorio Fault Zone in the Monterey Bay Region, California*, American Association of Petroleum Geologists, Pacific Section, Volume and Guidebook, GB-76, p. 53–74.
- TIMMS, N. E., HEALY, D., REYES-MONTES, J. M., COLLINS, D. S. PRIOR, D. J. & YOUNG, R. P. 2010. Effects of crystallographic anisotropy on fracture development and acoustic emission in quartz. *Journal of Geophysical Research*, **115**, B07202, doi:10.1029/2009JB006765.
- TREPMANN, C.A. 2008. Shock effects in quartz: compression versus shear deformation – An example from the Rochechouart impact structure, France. *Earth and Planetary Science Letters*, **267**, 322-332.
- VIGORITO, M., HURST, A., CARTWRIGHT, J.A. & SCOTT, A. 2008. Architecture of a sand injectite complex: implications for origin and timing. *Journal of the Geological Society, London*, **165**, 609-612.
- VIGORITO, M. & HURST, A. 2010. Regional sand injectite architecture as a record of pore pressure evolution and sand redistribution in the shallow crust: insights from the Panoche Giant Injection Complex, California. *Journal of the Geological Society, London*, **167**, 889-904.

WENK, H-R., JANSSEN, C., KENKMANN, T. & DRESEN, G. 2011. Mechancial twinning in quartz: Shock experiments, impact, pseudotachylites and fault breccias. *Tectonophyscs*, **510**, 69-79.

WILKINS, A.D., HURST, A., WILSON, M.J. & ARCHER, S. 2018. Palaeoenvironment in an ancient low-latitude, arid lacustrine basin with loessite: the Smith Bank Formation (early Triassic) in the Central North Sea Continental Shelf. *Sedimentology*, **65**, 335-359.

WU, F., HURST, A. & GRIPPA, A. 2018. Grain and pore micro-texture in sandstone sill and depositional sandstone reservoirs: preliminary insights. *Petroleum Geoscience*, **24**, 236–243.

ZVIRTES, G., HURST, A., PHILIPP, R.P, PALLADINO, G. & GRIPPA, A. 2019. The Tumey Giant Injection Complex, Tumey Hill, California (USA), *In: SILCOCK, S., (eds) UNSURE OF EDITORIAL LIST & TITLE*

ZVIRTES, G., PHILIPP, R.P, HURST, A., PALLADINO, G., DE ROS, D.F. & GRIPPA, A. 2020. Petrofacies of Eocene sand injectites of the Tumey Giant Injection Complex, California (USA). *Sedimentary Geology*, **400**,

ACCEPTED MANUSCRIPT



**Table 1.** Characteristics of micro-fractures in framework grains from sandstone intrusions. For brevity micro-fractures are referred to as fractures.

*Individual grains*

1. fractures are mostly arcuate with varying levels of curvature (Figs 1 to 5) irregular geometry is a composite of several arcuate fractures (Figs 3 & 4)
2. planar fractures are unusual and typically cleavage-related in feldspar (Fig. 1)
3. (micro-) hackles are preserved on some open fracture margins (Figs 3b & 4)
4. quartz and feldspar have similar-style fracturing (Figs 1c & d, 3); feldspar fractures along cleavage if their tensile strength is compromised by a pre-injection weakness, for example, partial alteration by weathering (Fig. 1a,b)
5. abundance of fractures varies in adjacent grains and in general (Figs 1c,d, 2)
6. fractures do not connect through adjacent grains, they stop at grain margins (Figs 1, 2a, 3)
7. fractured grains are not aligned or otherwise spatially organised (Fig. 1, 2a)
8. grains may be so intensely fractured that they appear to be agglomerations of silt-sized and finer grains (Fig. 2  $q_2$  &  $q_3$ )
9. open fractures that in 2D appear to transect entire grains (Figs. 1c, 3) when viewed in 3D probably do not (compare Figs 5a and b)
10. large (open) fractures taper (Figs 2a, 3 & 5b)
11. hairline fractures tend to be persistent and often form polygonal or radial patterns (Fig. 3)

*General*

1. closed fractures are only visible in petrographic thin sections (Fig. 1)
2. BSEM provides the clearest images
3. 3D images significantly enhance understanding of fracture geometry and persistence.



Fig. 1. Petrographic thin sections from sandstone sills (plane polarised light) from the Tumey Hill exposure of the mid-Eocene Tumey Giant Injection Complex (TGIC), Kreyenhagen Shale, California (modified from Zvirtes 2019). (a) Fine- to medium-grained, poorly sorted, feldspathic litharenite. Angular to sub-angular and poorly sorted grains. Quartz (**q**) has arcuate randomly oriented micro-fractures whereas feldspar (**f**) is intensely micro-fractured along cleavage and twin planes. Lithic grains (**l**) have less evidence of micro-fractures although chert (**ch**) is an exception. Of 28 sand-sized grains present: **q** = 5(2), **f** = 7, **ch** = 3, **l** = 2(9), in parenthesis are additional unfractured grains. (b) An adjacent sample from the same location as (a) with very similar textural features. Micro-fractures do not propagate into adjacent grains and are dissimilarly oriented. Of 32 sand-sized grains present: **q** = 7(5), **f** = 7, **ch** = 1, **l** = 4(8), in parenthesis are additional unfractured grains. (c) Detail of micro-fractured quartz in a fine-grained, poorly sorted, quartz litharenite with minor feldspar from the Right Angle Canyon exposure of the Danian PGIC (modified from Luzinski et al. 2019), emplaced into the Moreno Formation (Upper Cretaceous to Palaeocene), California (Vigorito & Hurst 2010). Fractures are planar, arcuate and irregular. Open micro-fractures have blue epoxy fill whereas closed micro-fractures dark brown. Micro-fractures do not propagate into adjacent grains and are dissimilarly oriented. (d) Micro-fractured feldspar with irregularly oriented open and closed fractures. Traces of cleavage-related fractures occur but are much less prominent than in (b) (modified from Luzinski et al. 2019).

Fig. 2. Micro-fractured quartz (**q**), feldspar (**f**) and areas of silt-sized grains (**si**) from the same PGIC sample in Fig. 1c and d (BSEM); **q**<sub>1</sub>, **q**<sub>2</sub>, **q**<sub>3</sub>, **q**<sub>4</sub>, **f**<sub>1</sub> and **si** are referred to in the main text. (a) Fine-grained and poorly sorted with numerous angular sand-sized grains, and some finer grains, with open fractures. White arrows show examples of serrate fracture margins. (b) Outlines of selected examples of micro-fractured grains and areas of silt-sized grains from (a). Fractures are predominantly irregular or arcuate and independent of mineralogy. Fracture along feldspar cleavage or twinning is very faint or absent.

Fig. 3. Micro-fracture characteristics in quartz grains in BSEM images. All grains are angular, have at least one large-aperture (up to at least 4  $\mu\text{m}$  across) micro-fracture and more numerous low aperture (<1  $\mu\text{m}$  across) micro-fractures. **a** Fracture geometry is predominantly irregular with subordinate arcuate form. Intense deformation and partial disintegration at the bottom left area of the grain, with locally intense hairline fractures, and large-aperture fractures along the zone of detachment. Black arrows indicate approximate directions of two normal-to-margin impacts. **b** A single wedge-shaped fracture within a background of irregular polygonal hairline fractures. **c** A large sawtooth fracture with associated smaller-aperture fractures. Similar PGIC location to Fig. 2.

Fig. 4. Micro-fractured feldspar grains (SEM, modified from Luzinski et al. 2019). (a) Pervasively fractured grain with apertures up to  $\sim 10 \mu\text{m}$  across. Fractures are planar (**p**), arcuate (**a**) and irregular. Jigsaw geometry is present along several opposing fracture surfaces, which in some cases preserves  $\mu\text{m}$ -scale hackles (**h**). Hairline fractures are rare. Diagenetic gypsum forms the planar surface mineralization. (b) A silt-sized grain with  $\mu\text{m}$ -aperture fractures and associated hairline fractures. Surface textures are numerous and complex, most prominently an array of sub- $\mu\text{m}$  scale hackles (**h**) on the right-hand surface. Similar PGIC location as in Fig. 2.

Fig. 5. Micro CT-scan (MCT) image of a sample from a sandstone sill in the PGIC, Right Angle Canyon (modified from Wu et al. 2018). (a) A circular 2D view through the sample (field of view is 1.45 mm across). Open micro-fractures are present in several grains (dark grey indicates low density, a proxy for porosity). (b) A single quartz grain in an extracted 3D volume (rectangle in (a)) that exhibits sub-angular grain morphology and several open fractures all of which terminate, or cannot be resolved, within the grain.

Fig. 6. Mudstone intraclasts from sandstone intrusions in the Santa Cruz Mudstone (late Miocene, Panther Beach), California (modified from Scott et al. 2009). (a) Sand-grain size mudstone clasts (**M**) along with micro-fractured sub-angular to sub-rounded quartz, abundant lithic grains and less common feldspar. Note the “jigsaw” texture in a mudstone grain near the centre-field of view (plane polarised light). (B) BSEM image of a sandstone with  $\sim 40\%$  low density mudstone clasts (black). Several angular quartz and feldspar grains have clearly visible open fractures.

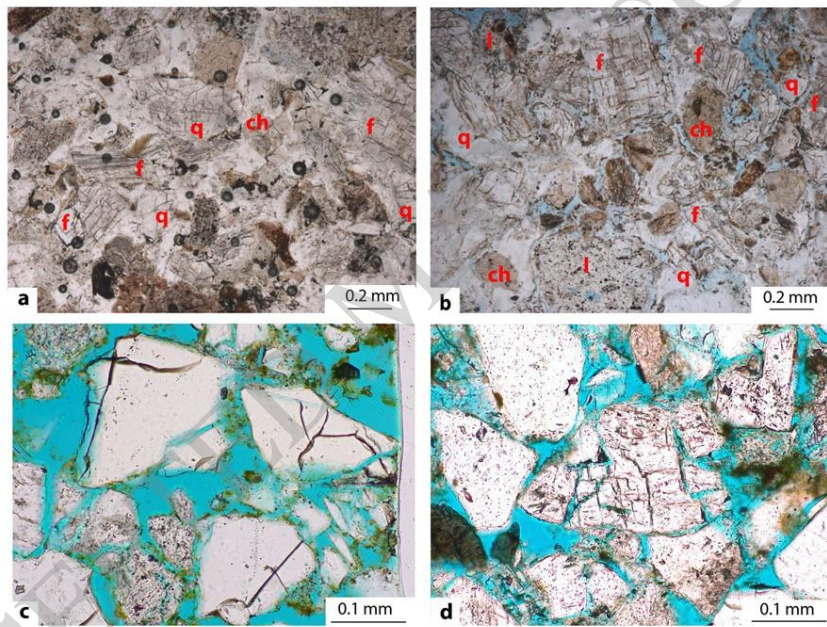
Fig. 7. (a) A large mudstone clast ( $>7 \text{ mm}$  across) from the late Miocene at Panther Beach (see Fig. 6). A  $>3 \text{ mm}$  long, up to  $\sim 0.2 \text{ mm}$  aperture sand-filled fracture (*i*) extends almost halfway across the field of view. Several incipient ( $<0.4 \text{ mm}$  long) sand-filled fractures occur (*ii*) and a possible oblique section through a larger fracture (*iii*). Margins of the clast are predominantly extremely diffuse, where sand grains are mixed with the mudstone clast (*iv*). Relatively planar abrupt transitions from mud to sand (*v*) are less common. (b) Sketch of main features in (a). The grain boundary (red; the grain is larger than the field of view) and all sand-filled fractures are outlined in black; solid, dashed and dotted lines indicate decreasing levels of clarity.

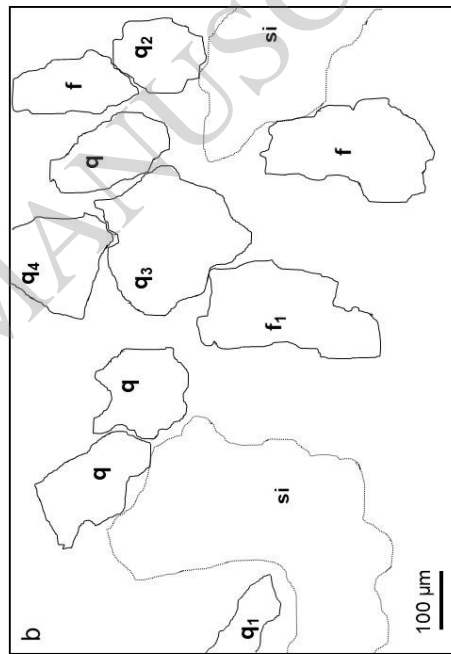
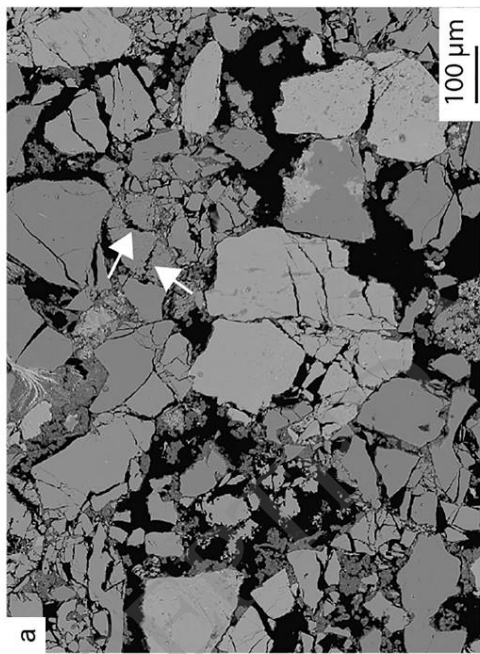
Fig. 8. (a) Effect of abrasion on ATi (apatite:tourmaline ratio) in depositional parent units, the intrusive complex and, sand extrudites in the Panoche Giant Injection Complex (PGIC, Danian). Note that in the intrusive complex weathering-controlled dissolution of apatite occurred (from data in Fig. 3, Hurst et al. 2017). (b) Relative hardness of selected heavy minerals (Mohs scale) in relation to quartz (**Q**) and feldspar (**F**): **Ap**, apatite; **Sp**, titanite; **Ep**,

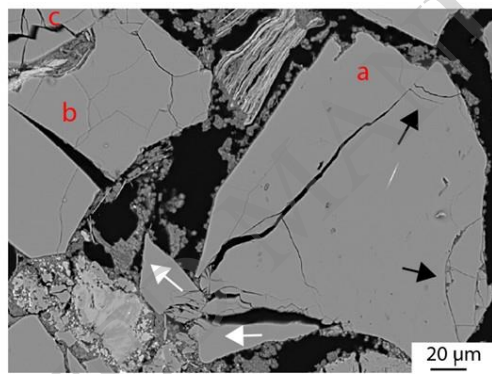
epidote; Gt, garnet (andradite–grossular  $h < 7$ ); St, staurolite; **To**, tourmaline; Zr, zircon; Cr, chrome-spinel; An, andalusite; Ru, rutile; At, anatase; Ca, calcic amphibole; and Mo, monazite (modified after Hurst et al. 2017).

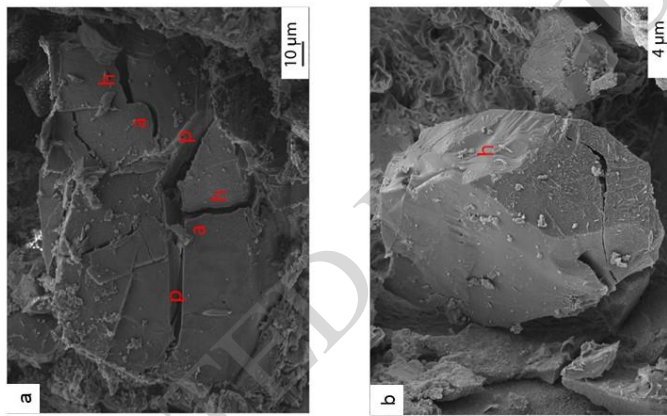
Fig. 9. Hydrodynamic fraction of zircon relative to tourmaline in the PGIC, Moreno Gulch. Zircon and tourmaline are similarly durable but high and low density, respectively. (a) ZTi (zircon-tourmaline index) in stratigraphic section as shown on the accompanying figure. (b) Sample locations. Strata dip at  $\sim 30^\circ$  to the northeast and young from left to right. Image from Google Earth. Adapted from Hurst et al. (2017).

ACCEPTED MANUSCRIPT

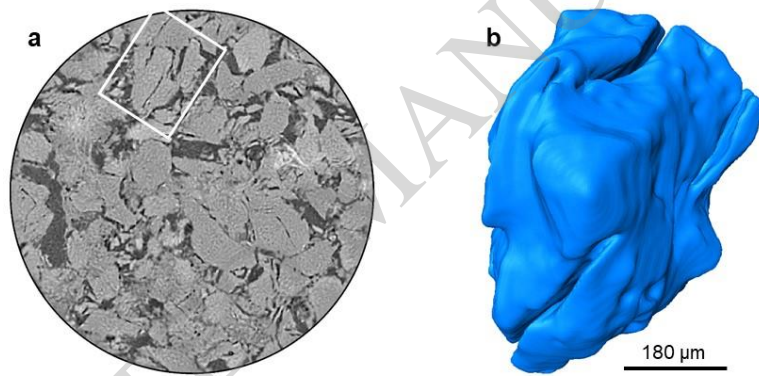




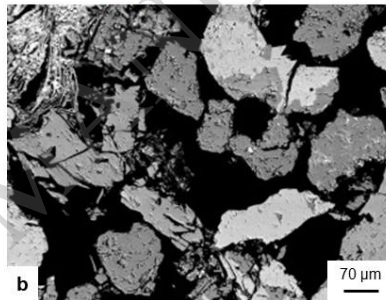
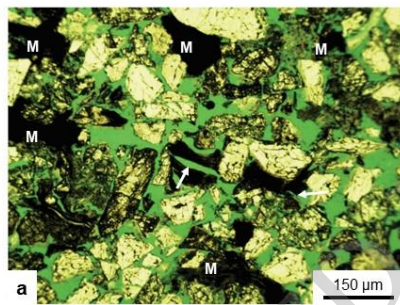


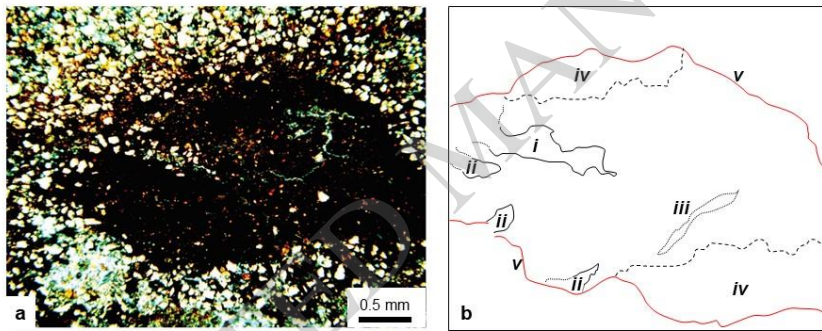


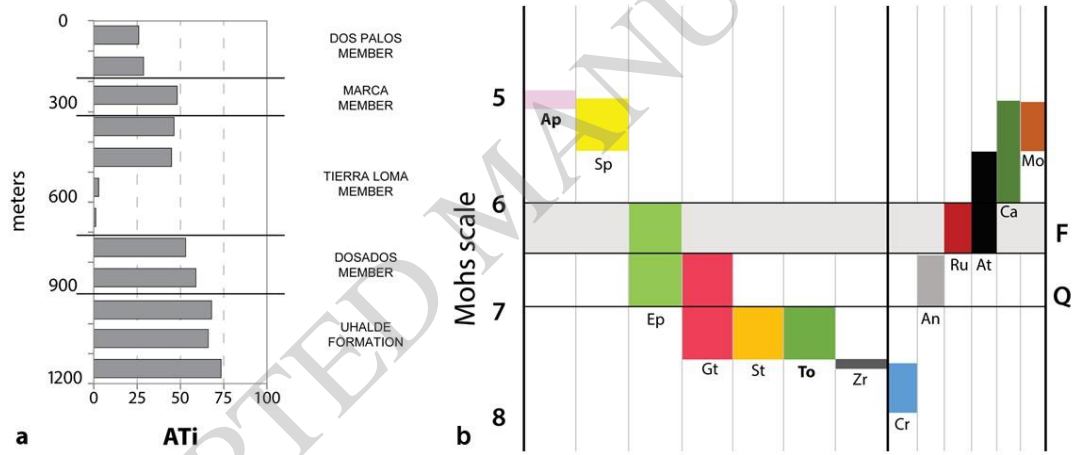












ACCEPTED MANUSCRIPT

